A Soft Magnetic Core can Enhance Navigation Performance of Magnetic Nanoparticles in Targeted Drug Delivery

Xingming Zhang, Tuan-Anh Le, Ali Kafash Hoshiar, and Jungwon Yoon, *Member, IEEE*

***Abstract*—Magnetic nanoparticles (MNPs) are a promising candidate for use as carriers in drug delivery systems. A navigation system with real-time actuation and monitoring of MNPs is inevitably required for more precise targeting and diagnosis. In this paper, we propose a novel electromagnetic navigation system with a coil combined with a soft magnetic core. This system can be used for magnetic particle imaging (MPI) and electromagnetic actuator functions with a higher steering force and enhanced monitoring resolution. A soft magnetic core with coils can increase the magnetic gradient field. However, this also generates harmonic noise, which makes it difficult to acquire MNP monitoring signals with MPI. Therefore, the use of amplitude modulation magnetic particle imaging (AM MPI) is suggested. AM MPI uses a low-amplitude excitation field combined with a low-frequency drive field. Using this system, the measured signal becomes less sensitive to the soft magnetic core. Based on the new MPI scheme and the combination of the coil with the magnetic cores, the proposed navigation system can implement one-dimensional (1-D) MNP navigation and 2-D MPI. The proposed navigation system can shorten the 1-D guidance time by about 25% for MNPs in the size range of 45–60 nm and give an improved 2-D imaging resolution of 43%, compared with an air-coil structure.**

***Index Terms*—Magnetic particlei (MPI), magnetic nanoparticles (MNPs), navigation resolution, soft magnetic core.**

Manuscript received May 11, 2017; revised October 25, 2017 and March 9, 2018; accepted May 19, 2018. Date of publication June 4, 2018; date of current version August 14, 2018. Recommended by Technical Editor Professor Weihua (MCPS) Li. This work was supported in part by the National Research Foundation of Korea under Grant 2017R1A2B4011704 and Grant 2018M3C1B8017773, and in part by the Fundamental Research Funds for the Central Universities under Grant HIT.NSRIF.2018065. *(Xingming Zhang and Tuan-Anh Le contributed equally to this work.) (Corresponding author: Jungwon Yoon.)*

X. Zhang is with the School of Naval Architecture and Ocean Engineering, Harbin Institute of Technology at Weihai, Weihai, Shandong 264209, China, and also with the Institute of Science and Technology, Gwangju 500-712, South Korea (e-mail: zhxm@hit.edu.cn).

T. -A Le and J. Yoon are with the School of Integrated Technology, Gwangju Institute of Science and Technology, Gwangju 500-712, South Korea (e-mail: tuananhle@gist.ac.kr; jyoon@gist.ac.kr).

A. K. Hoshiar is with the Faculty of Industrial and Mechanical Engineering, Islamic Azad University, Qazvin Branch, Qazvin 34199-15195, Iran (e-mail: hoshiar@QIAU.ac.ir).

Color versions of one or more of the figures in this paper are available online at http://ieeexplore.ieee.org.

Digital Object Identifier 10.1109/TMECH.2018.2843820

I. Introduction

MAGNETIC nanoparticles (MNPs) that can be manipulated using magnetic fields can function at both the cellular and the molecular levels [1]. This makes them suitable for use as carriers for targeted drug delivery (TDD) and contrast agents in magnetic particle imaging (MPI) [2]. Although traditionally delivered drugs reach their target locations, they also affect healthy tissues causing undesirable side effects. Thus, TDD systems have been developed to enhance the efficiency of treatment and maintain optimal doses at the desired location [3]. In TDD, therapeutic magnetizable particles are injected, generally into blood vessels, and external magnets are used to guide and concentrate them at the diseased target organ [4], [5]. In recent work, we conducted extensive *in vivo* experiments to demonstrate the effectiveness of an electromagnetic actuator (EMA) based on open-loop control for the delivery of MNPs to mouse brains [6]. However, we must also be able to track the nanoparticles in TDD. This would allow for more precise targeting and diagnosis based on the spatial layout of the nanoparticles.

Several methods have been suggested for developing TDD with a feedback scheme such as using ultrasound to locate solid micro-particles [7], using a microscope or an optical camera to track visible particles [8], [9], or using a magnetic resonance imaging (MRI) system [10]–[13]. The groundbreaking magnetic resonance navigation (MRN) system proposed by Martel *et al.* [10], [11] includes a feedback control scheme. In MRN, embedded microparticles are tracked by MRI systems and controlled by additional electromagnetic coils. This scheme is used because the magnetic field gradient in MRI systems is limited to a maximum of 400 mT/m/μ_0, which is not sufficient for remote control of the MNPs [14].

MPI is a fast and sensitive imaging modality that is used to measure the spatial distribution of MNPs [2]. MPI systems offer spatial resolutions on the millimeter scale and high temporal resolutions, with about 45 three-dimensional (3-D) volumes/s [2]. The high temporal and spatial resolution of MPI fulfills the requirements for cardiovascular, neurological, and peripheral vascular applications [15], [16]. In addition, the detection threshold of MNPs is less impaired by background signals from the host tissue compared to MRI. Tracer MNPs in MPI can provide spatial information and can also be used as drug carrier particles. When adopting MNPs of 50-nm core size, with a 5.1 T/m/μ_0 magnetic field gradient, potential resolutions of up to 0.11 mm can be achieved [17]. Therefore, a real-time navigation system for MNPs based on MPI is capable of performing actuation and monitoring tasks simultaneously. This has particular application in precise steering and tracking of MNPs with real-time feedback schemes for drug delivery to the brain.

The control performance of MPI-based navigation systems mainly depends on the magnetic field gradient of both the EMA and the MPI. The former determines the magnitude of the steering force for manipulation of nanosized particles and the latter determines the resolution of the MPI image. Cherry *et al.* [18] showed that the magnetic force acting on MNPs using standard magnetic actuation systems cannot deliver them to brain cells due to their nanosize. For monitoring of specified nanoparticles, the full-width at half-maximum (FWHM) resolution of MPI is proportional to the reciprocal of the gradient [17]. Therefore, a larger magnetic field gradient should be considered to increase both the steering force and the image quality for MNP monitoring.

One typical method for increasing the gradient field is to increase the size of the coil or to use superconductivity. However, a compact and efficient way to increase the gradient field is utilization of a soft magnetic material core. Soft magnetic cores, which are easily magnetized and demagnetized, can enhance the field strength and gradient [19]. Latulippe *et al.* [20] proposed the concept of dipole field navigation, which utilizes ferromagnetic cores in an MRI scanner to generate high field gradients. However, soft magnetic materials exhibit a nonlinear magnetization response and are not suitable for the original MPI scheme [2]. A soft magnetic material exposed to a high-frequency and high-amplitude magnetic field generates a harmonic distortion, which will screen the particles' signal during the MPI process. Furthermore, the original MPI scheme has some limitations, including a dramatic reduction in the magnetic field strength and the magnetic gradient [21], the possibility of unpleasant peripheral nerve stimulation (PNS) [22], [23], and a wide-bandwidth receiver coil [23] with expensive and bulky components.

In this paper, we introduce a novel navigation system for MNPs based on an MPI system enhanced by soft magnetic cores. The proposed system can provide a real-time MNP guidance scheme for TDD with enhanced actuation and monitoring performance. In the proposed MPI system, we utilize a low-frequency field to move the field-free point (FFP), and employ a low-amplitude field at high frequency to oscillate the magnetization near the FFP. As the amplitude of the received signal is used to reconstruct the MPI images, the proposed MPI system, called amplitude modulation magnetic particle imaging (AM MPI), utilizes the iron cores available to perform the MPI function with a higher gradient to achieve a larger workspace with relatively simple hardware components.

Therefore, the proposed method can enhance both the image quality and steering magnetic force for higher manipulability of MNPs. In this paper, we propose an MPI-based 1-D navigation system with iron cores. The effects of iron cores on EMA and MPI periods are discussed in detail, and the proposed MPI-based navigation system is demonstrated through 1-D guidance tests to show that the iron cores can enhance the steering force of MNPs. Finally, a mechanical scanner is used to demonstrate that a 2-D map of MNP distribution exhibits better image quality.

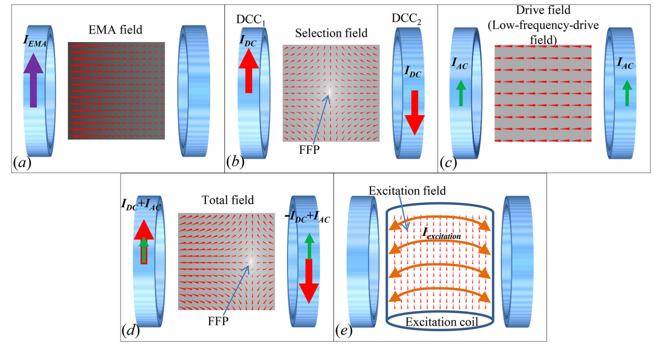

Fig. 1. Functional magnetic fields generated by different currents in the workspace. The grayscale and the length of the cones represent the magnitude of the field strength, while the direction of the cone indicates the direction of the field. (a) During the EMA period, the EMA field, which is a gradient field used to steer the MNPs, is induced by current I_{EMA} in the DCC. (b) FFP is located at the center of the selection field, which is generated by current I_{DC} in the opposite direction. (c) Drive field is a homogeneous field generated by same-direction currents I_{AC} in the coils. (d) Effect of I_{DC} and I_{AC} causes the FPP to move. (e) Excitation field is generated by the excitation coil with a high-frequency current $I_{\mathrm{excitation}}$, it has a small amplitude compared to the selection and drive fields, andthe position of the FFP can be considered to be independent of the excitation field.

II. Navigation System of MNPs

In our previous work [24], [25], we introduced a hybrid navigation system concept comprised of an EMA mode and an MPI mode. The coil topology was composed of air-core coils as shown in Fig. 1(a). In EMA mode, one of the differential-current coils (DCCs) [19] loads the current I_{EMA} to generate the magnetic field gradient [see Fig. 1(a)], which can steer the MNPs toward the current-carrying coil. In MPI mode, the DCCs load two currents I_{DC} that have equal amplitude but opposite directions to generate a selection field as well as an FFP [see Fig. 1(b)]. The FFP shift is achieved by the superposition of the static selection field and the time-varying drive field. The drive field induced by I_{AC} is spatially homogeneous at any given moment [see Fig. 1(c) and (d)]. The DCCs combine each coil for the low-frequency drive field (frequencies ranging from 0 to 100 Hz) and for the selection field into one set of coils. The excitation field, a high-frequency field with frequencies in the range of 10–100 kHz, is employed to oscillate the magnetization of the particles and then to generate the signal, as shown in Fig. 1(e).

Real-time MPI and EMA in the proposed navigation system can be achieved by applying a time-division multiplexing scheme to the coil topology [24]. This can integrate the EMA and MPI tasks through time sequencing. Every navigation period consists of at least one MPI scanning period to detect MNP positions and one EMA period to control MNP positions. During the EMA mode, magnetic fields will be high enough to steer MNPs, which results in MNP saturation. However, the MNPs must be demagnetized before MPI mode. Furthermore, owing

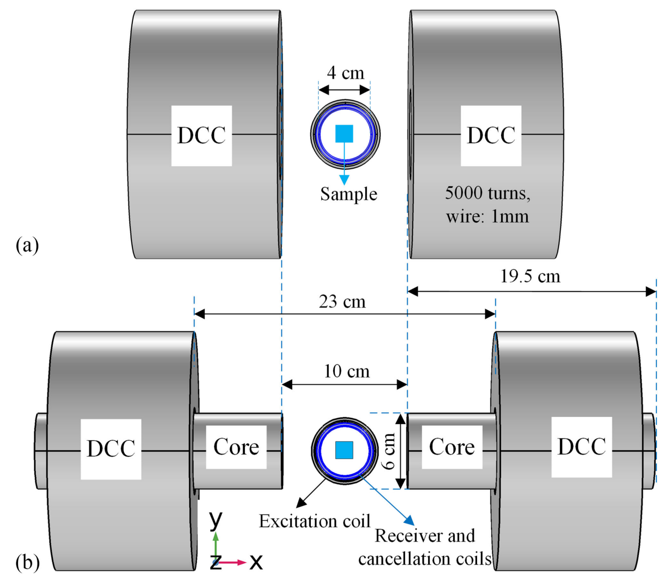

Fig. 2. Installation of a soft core into the hollow coil in a navigation system. (a) Air-core coil navigation system; the DCCs are the hollow coils. (b) Core-coil navigation system; the iron core is installed inside the hollow coils. Both systems have the same combination of signal receiver coil and field excitation coil. These are placed between the DCCs. The size of the workspaces and the gaps between the DCCs are set to the same values: 4 cm and 10 cm, respectively. Each cylindrical core is 19.5 cm in length and 6 cm in diameter. The sample to be tested is placed in the receiver coil.

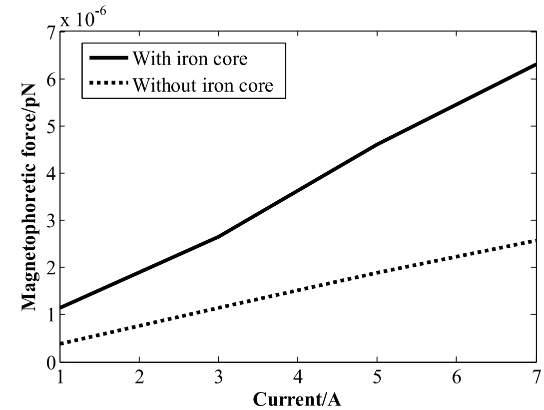

Fig. 3. Magnetophoretic force applied on a Resovist particle placed at the center of the system.

to the high impedance of coils, the currents in coils cannot be changed immediately between EMA and MPI modes. Therefore, a relaxation period is introduced for demagnetization of MNPs and prevention of a voltage surge from the coils. During MPI mode, the alternating magnetic field may affect MNP positions; however, our previous work demonstrated that the force factor during the MPI cycle has little effect on the position of the MNPs compared to their motion during the EMA mode [25] due to the alternating characteristics. Therefore, MPI mode operates during an off-cycle period in the actuation duty cycle for navigation control.

Because each gradient field in EMA and MPI mode plays a key role in enhancing navigation performance, in this paper, we propose the installation of a soft core into the hollow coil of an existing navigation system, as shown in Fig. 2. The gradient fields of a navigation system with iron cores are compared to a navigation system with air cores in subsequent sections. In Fig. 2, the center of the signal receiver coil is defined as the coordinate origin, the axis of the DCCs is the x-axis, and the axis of the receiver coil is the z-axis.

III. Iron Core for Magnetophoretic Force

The MNPs in the workspace are saturated and steered by a gradient magnetic field induced by I_{EMA} during the EMA period, as shown in Fig. 1(a). The magnetophoretic force on MNPs is given by

$$F_m = \mu_0 v_p M_s \cdot \nabla H \tag{1}$$

where μ_0 is the vacuum permeability, v_p is the core volume of MNPs, M_s is the saturation magnetization, and ∇H is the gradient of the magnetic field. The saturation force is proportional to the gradient, which can be enhanced by the iron core.

The main material used in MNPs is magnetite (Fe_3O_4). Different-sized MNPs have different magnetite magnetization curves. The magnetic field required to fully saturate the MNPs is too large, such as it is with magnetite powder at room temperature [19] or several different samples of magnetite at 5 K [26]. The magnetic field required to saturate MNPs is about 1.63 T/μ_0 ($\sim$16 kOe). However, owing to the nonlinear shape of the magnetization, a lower magnetic field of about 0.126 T/μ_0 ($\sim$1.2 kOe), which is only 8% of the magnetic intensity required for saturation, can magnetize the magnetite until 74% of the saturated magnetization [19], [26]. Since this medium-range magnetic field can generate sufficient magnetization in the particles, therefore, generation of a higher gradient will be more effective. Because an increased number of turns and/or current in the coils to induce the higher gradient field require larger and heavier coils, using the cores inside the coils to amplify the magnetic field is a compact and energy-efficient method.

To improve the efficiency of the electromagnets for MNP guidance in EMA mode, structural parameters of the cores and coils were chosen based on simulation results to provide the highest magnetic force in the region of interest (ROI), which was set at the size of a mouse brain [19]. We considered the width and height of the coil and the wire diameter while designing the system. We also considered the distance between cores with respect to both the magnetic field strength and gradient. Minimum radius of the cores and the tip length had only a minor influence on the gradient and the magnetic strength. Certain constraints such as the output power supply and inner and outer coil diameters should also be considered in the system design. Based on these constraints and the simulation results, the optimum configuration was chosen to satisfy the largest minimum force factor in the ROI [19] [see Fig. 2(b)]. The analytical results for the magnetophoretic force applied to a Resovist particle (Meito Sangyo Co., Ltd.) placed at the center of the system are also shown in Fig. 3. In this paper, the Resovist particle is

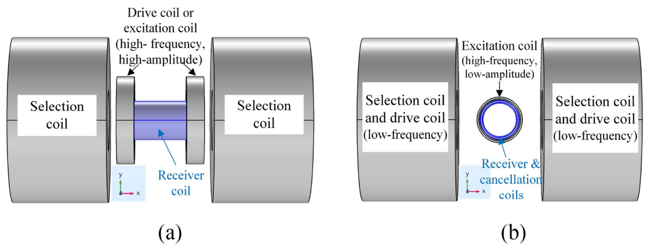

Fig. 4. Comparison of MPI schemes. (a) Original MPI. (b) Proposed AM MPI scheme.

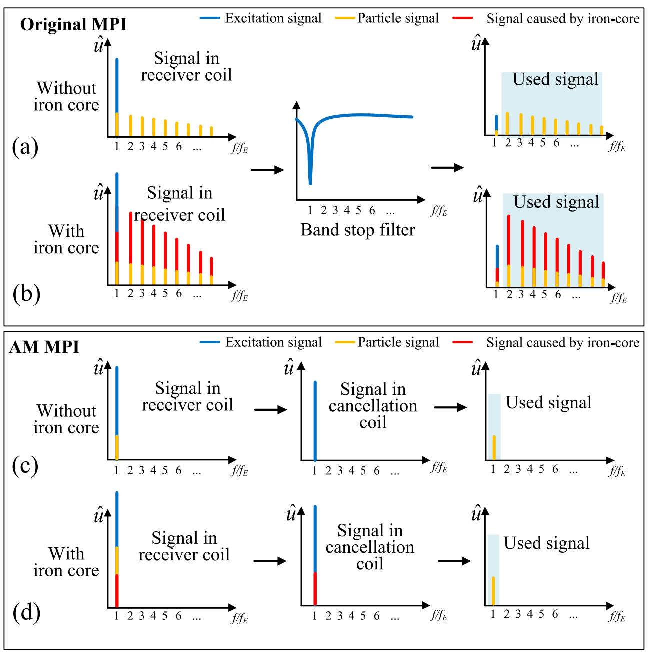

Fig. 5. Fourier coefficients for each method, with a logarithmic scale for the signal. (a) Original MPI method without iron core. (b) Original MPI method with iron core. (c) AM MPI method without iron core. (d) AM MPI method with iron core.

considered to have an effective aggregation diameter of 24 nm [27]. As such, a cylindrical core structure can significantly strengthen the magnetic field and its gradient at the ROI by about 2.3 times of the magnetophoretic force.

IV. Iron-Core-Compatible MPI Scheme

A. Comparisons Between the Original MPI Scheme and The Proposed AM MPI Scheme

The original MPI and proposed AM MPI schemes are shown in Fig. 4. In the case of the original MPI scheme, the required high-frequency and high-amplitude magnetic drive field causes that the harmonics induced by the soft magnetic material components become much larger than the harmonics induced by the MNPs, which usually have a much smaller effective iron-content than the soft magnetic components. These harmonics screen the signal from the particles during the MPI process (shown in Fig. 5(a) and (b)). The drive field is even reduced significantly when the soft cores are isolated by shielding plates. Thus, much information is lost in MPI images taken using the conventional filter method [28].

On the other hand, the proposed AM MPI employs a low-frequency field (referred to as the low-frequency drive field) and a high-frequency, low-amplitude field (which we call the excitation field in this paper). The low-frequency component of the signal can easily be eliminated by using a high-pass filter. When there are no MNPs inside the field of view, the excitation field and iron cores can affect the amplitude of the high-frequency component, as shown in Fig. 5(c) and (d), while the high-frequency voltage is cancelled out by the receiver coil and the cancellation coil, which are connected in series [28], [29]. As the coils have the same geometry but are wound in the opposite direction, the total output is dominated by the MNPs. Moreover, the AM MPI can easily be extended to 3-D imaging because only one pair is required for the receiver-cancellation coil.

Therefore, the use of soft magnetic cores confers the following three major advantages to the proposed AM MPI.

1) Our proposed system uses a low-amplitude excitation field combined with a low-frequency drive field. This means that the harmonic distortions will have little effect, and a simple cancellation method can be applied to create a 3-D MPI. Thus, the iron cores can be used in an MPI with a higher gradient field.
2) As the low-amplitude excitation field has a frequency of 40 kHz and an amplitude of 200 μT, the possibility of PNS is significantly reduced.
3) The AM MPI uses a narrow-band receiver coil, facilitating impedance match design and eliminating noise from other frequencies.

B. Signal Produced by the Original MPI

The original MPI scheme relies on the nonlinearity of the MNP magnetization curves with the MNP magnetization saturated with the saturation field strength. The relationship between the magnetization of the particles and the outer magnetic field can be described using Langevin theory of paramagnetism [2]

$$M = cv_p M_s L\left[\frac{mH}{k_B T}\right] = cv_p M_s\left[\coth\left(\frac{mH}{k_B T}\right) - \frac{k_B T}{mH}\right] \tag{2}$$

where L is the Langevin function, in particular $L(0) = 0$, M_S is the saturation magnetization of the particle, v_p is the volume of core particles, c is the concentration of particles, H is the applied magnetic field, k_B is the Boltzmann constant, m is the magnetic moment of a single MNP, and T is the particle temperature.

It is assumed that the sample is in a 1-D shape along the x-axis and that the concentration of particles is $c(x)$ along the sample. The MPI only scans the sample in the x-direction. For the original 1-D MPI concept, the target is exposed to a selection field. The magnetic field strength gradient of the selection field along the x-axis is G_x, and a single frequency sinusoidal drive field $H_D(t)$ is applied. The signal generated by the oscillating magnetized particles can be described as

$$u_P(t) = -p_{Rx}\dot{H}_D(t)(c * \tilde{m})\left[-G_x^{-1}H_D(t)\right] \tag{3}$$

where $H_D(t)$ is the drive field used for FFP movement and generation of the particle signal by oscillating the magnetization of the particles, and p_{Rx} denotes the receiver coil sensitivity along the *x*-axis, which contains all geometrical parameters of the receiver coil. $\tilde{m}(x) = \mu_0 \dot{\bar{m}}(G_x x)$, where $\dot{\bar{m}}$ denotes the derivative of the mean magnetic moment. The operator $*$ is the convolution of two functions. According to the coordinate transform introduced in [28], we obtain the position of the FFP

$$x_{\text{FFP}}(t) = -G_x^{-1} H_D\left(t\right). \tag{4}$$

The signal of (3) can be received by a receiver coil. The strong signal excluding particles can be isolated by a band-stop filter [28]. The filtered signals indicate the concentration of nanoparticles. By combining the concentration information with the acquired signal, the nanoparticle spatial distribution can be reconstructed into an image.

C. Signal Produced by Core-Compatible MPI

For the proposed MPI scheme, the selection field is identical to that in the original MPI scheme and the selection field is generated by I_{DC}, as shown in Fig. 1(b). However, the sinusoidal drive field signal in the original MPI is separated into two sinusoidal fields of different frequencies, which are perpendicular to each other along the *x* and *z*-axes with coils setup as Fig. 4(b). The first field is a low-frequency drive field with a high amplitude to move only the FFP along the *x*-axis, generated by I_{AC} [see Fig. 1(d)]. The other is a high-frequency excitation field with a low amplitude that is used to oscillate the magnetization of the particles and then to generate the signal [see Fig. 1(e)]. If the MNPs are saturated and magnetized by the strong field, the excitation field cannot change the magnetization status of these MNPs due to its weak magnitude, and these MNPs also cannot generate any signal. Therefore, if the MNPs are only located at or near the FFP, the excitation field can generate a signal with an existing selection field. Consequently, the total field in the proposed MPI (similar to the drive field in original MPI) is separately given by

$$\boldsymbol{H}(t) = A_D \cos(2\pi f_D t)\mathbf{e}_x + A_E \cos(2\pi f_E t)\mathbf{e}_z \tag{5}$$

where A_D and A_E are the amplitudes of the low-frequency drive field and the excitation field, respectively, f_D and f_E are field frequencies, and $\boldsymbol{e}_x$ and $\boldsymbol{e}_z$ are unit vectors in the *x* and z-axes, respectively.

We assume that $A_E << A_D$, $f_E >> f_D$, and $A_E f_E >> A_D f_{\text{D}}$. Since magnitude of the total field is given by the low-frequency drive field, the total field and its derivative from (5) can be represented as follows:

$$\boldsymbol{H}(t) \approx A_D \cos(2\pi f_D t)\mathbf{e}_x \tag{6}$$

$$\dot{\boldsymbol{H}}(t) = -2\pi f_D A_D \sin(2\pi f_D t)\mathbf{e}_x - 2\pi f_E A_E \sin(2\pi f_E t)\mathbf{e}_z. \tag{7}$$

In (3), if we replace $H_{\text{D}}(t)$ and $\dot{H}_D(t)$ by $\boldsymbol{H}(t)$ and $\dot{\boldsymbol{H}}(t)$ from (6) and (7), respectively, the voltage induced by the particles can be rewritten as

$$\boldsymbol{u}_P(t) \approx u_{PL}(t)\mathbf{e}_x + u_{PH}(t)\mathbf{e}_z \tag{8}$$

where

$$\begin{aligned} u_{PL}(t) = {} & 2\pi p_{Rx} A_D f_D \sin(2\pi f_D t) \\ & \cdot(c * \tilde{m})\left[-G_x^{-1} A_D \cos(2\pi f_D t)\right] \end{aligned} \tag{9}$$

$$\begin{aligned} u_{PH}(t) = {} & 2\pi p_{Rz} A_E f_E \sin(2\pi f_E t) \\ & \cdot(c * \tilde{m})\left[-G_x^{-1} A_D \cos(2\pi f_D t)\right] \end{aligned} \tag{10}$$

p_{Rz} denotes the receiver coil sensitivity along *z*-axis, $u_{PL}(t)$ is the low-frequency component of the particle signal caused by the FFP movement, and $u_{PH}(t)$ is the high-frequency component of the particle signal caused by the excitation frequency f_E. In (4), if we replace $H_{\text{D}}(t)$ by $H(t)$ from (6), we obtain the position of the FFP

$$\boldsymbol{x}_{\text{FFP}}(t) \approx -G_x^{-1} A_D \cos(2\pi f_D t)\mathbf{e}_x. \tag{11}$$

Equation (11) indicates that the FFP moves in the *x*-direction, and its position depends on the amplitude of the low-frequency drive field and the gradient of the selection field. The time signals (8)–(10) can be mapped onto a spatial interval and described by an ordinary convolution

$$\boldsymbol{u}_P\left[x_{\text{FFP}}(t)\right] \approx u_{PL}\left[x_{\text{FFP}}(t)\right]\mathbf{e}_x + u_{PH}\left[x_{\text{FFP}}(t)\right]\mathbf{e}_z. \tag{12}$$

Equations (9) and (10) can be converted into

$$u_{PL}\left[x_{\text{FFP}}(t)\right] = 2\pi p_{Rx} A_D f_D \left(c * \tilde{m}\right)\left[x_{\text{FFP}}(t)\right] \sin\left(2\pi f_D t\right) \tag{13}$$

$$u_{PH}\left[x_{\text{FFP}}(t)\right] = 2\pi p_{Rz} A_E f_E \left(c * \tilde{m}\right)\left[x_{\text{FFP}}(t)\right] \sin\left(2\pi f_E t\right). \tag{14}$$

Since $u_{PH}(t) >> u_{PL}(t)$, u_{PH} is used to reconstruct the MPI images. Moreover, the higher excitation frequency will improve the signal-to-noise-ratio [30]. If we align the excitation and receiver coils along the z-axis, we can receive u_{PH} only. Equation (14) indicates that the high-frequency signal is a sinusoidal voltage under the frequency f_E, with an amplitude proportional to the particle concentration at the FFP and the amplitude and frequency of the excitation field. Equation (14) also implies that we need to know the amplitude of u_{PH} to reconstruct the MPI images from the AM MPI.

D. Signal Processing and Reconstruction of the Core-Compatible MPI

A signal processing procedure for determining the particle concentration is described in Fig. 6. When the excitation coil in MPI is supplied by a low-current circuit, the high-frequency and low-amplitude excitation field is induced for magnetization of the MNPs. Then, the magnetized particles generate the signal, which will be received by a receiver coil. The excitation field coupled to the receiver coil also induces a signal with an excitation frequency. This signal, which exists even when the receiver coil has no MNPs inside, is called the excitation signal $u_E'(t)$. The excitation signal is measured when no MNPs are located inside the receiver coil and should be eliminated by a cancellation coil [29]. The excitation field will induce ac voltages in both coils ($u_E'(t)$ in the receiver coil and $u_C(t)$ in the cancellation coil) due to Faraday's law. Due to their identical geometric parameters, the induced voltages in the two coils have the same

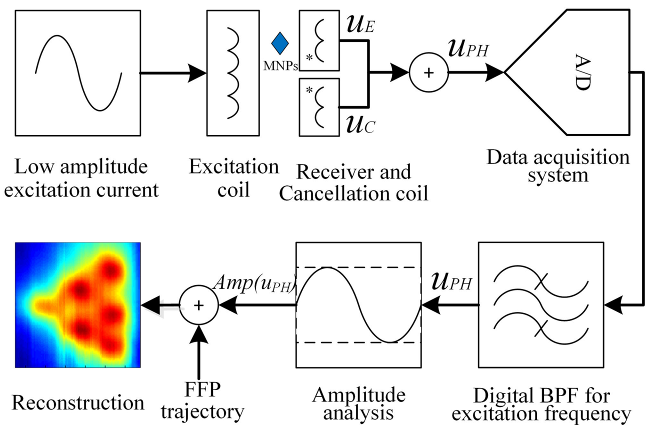

Fig. 6. Signal flow diagram of the realized set-up.

amplitudes but opposite directions (or $u'_E(t) \approx -u_C(t)$), resulting in the cancellation of both voltage phases. Thus, the total voltage of the receiver coil and the cancellation coil is reduced to approximately 0 V. When there are MNPs located inside the receiver coil, the particle signal is included in the excitation signal, which becomes $u_E(t)$

$$u_E(t) = u'_E(t) + u_p(t). \tag{15}$$

Then, we can measure the particle signal $u_P(t)$ by combining the signals from the receiver coil and the cancellation coil as follows:

$$u_P(t) \approx u_E(t) + u_C(t). \tag{16}$$

The particle signal can be digitized using a DAQ acquisition system. The signal can then be filtered using a band-pass filter that determines the high-frequency components of the signal (u_{PH}) with a narrow-band frequency. Therefore, a narrow-band receiver coil for the excitation frequency is sufficient for acquiring the particle signal. According to (14), the amplitude of the filtered signal contains information on particle concentration at the FFP. The amplitude of the signal is as follows:

$$\text{Amp}\left[u_{PH}(x_{\text{FFP}})\right] = 2\pi p_{Rz} A_E f_E (c * \tilde{m})\left[x_{\text{FFP}}\right]. \tag{17}$$

For an MPI system, A_E, f_E, and p_{Rz} are constants and the amplitude of the high-frequency signal component depends only on the density of the MNPs. Thus, we can easily reconstruct this signal combined with the present trajectory of the FFP. Once we have measured the MPI signal, we can generate an AM MPI image by gridding the received signal to the instantaneous position of the FFP. The resulting image can then be reconstructed using

$$\text{IMG}(x) = \text{Amp}\left[u_{PH}(x)\right] \tag{18}$$

where x is the position of the FFP. According to (18), the value of every pixel in the AM MPI image is the amplitude of the high-frequency signal when the FFP arrives.

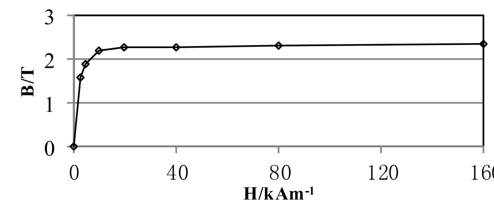

Fig. 7. B–H curve of VACOFLUX 50.

TABLE I
COIL SPECIFICATIONS

	Turns	*Inner diameter*	*Outer diameter*	*Coil length*	*Wire*
DCC	5000 each	7 cm	19 cm	7 cm	1 mm copper wire
Receiver coil	400	4.2 cm	Single layer	6 cm	Litz wire
Cancellation coil	200 each	4.2 cm	Single layer	1.5 cm	Litz wire
Excitation coil	44	5 cm	Single layer	11 cm	Litz wire

V. IRON CORES IN MPI

According to the proposed AM MPI scheme, the soft iron cores can be used in a navigation system for MNPs. We will now discuss the implementation of the proposed MPI scheme in detail.

A. Simulation and Experimental Setup for Investigating the Coil-Core Structure

The structural parameters of the cores and coils in Fig. 2 are suitable for enhancing the gradient of the selection field when the system is operating in MPI mode. However, we must also consider the effect of the frequency on the behavior of the magnetic material when the system is operating in this mode (alternating current (ac) applications). In this respect, materials with a very high saturation, low-coercive field strength, and low specific core losses are desirable, as these limit the impact of the iron core on the MPI operation. The iron core in our electromagnetic actuation system is composed of a soft magnetic alloy, VACOFLUX 50 (Vacuumschmelze) as a MPI compatible material [31], its B–H curve is shown in Fig. 7.

Moreover, the remanence has less effect on the MPI, as during MPI, each coil loads I_{DC} and I_{AC}. As I_{DC} is always larger than I_{AC}, the cores are always magnetized in one direction so the conditions required for remanence do not occur. As we have taken the relaxation time into account, the steering of the MNPs will not be affected by the remanence either.

For comparison and objective analysis of the electromagnetic systems with the iron-core coil and with the air-core coil, the size of the workspaces and the gap between DCCs were set to the same values, as shown in Fig. 2. The coil parameters are shown in Table I for both simulation and experiments. We

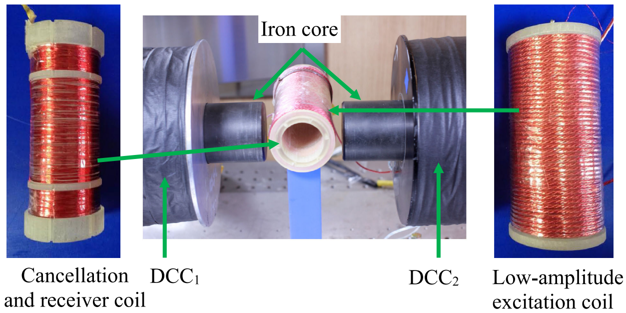

Fig. 8. Experimental set-up for hybrid electromagnetic MNP actuation and imaging with an iron core.

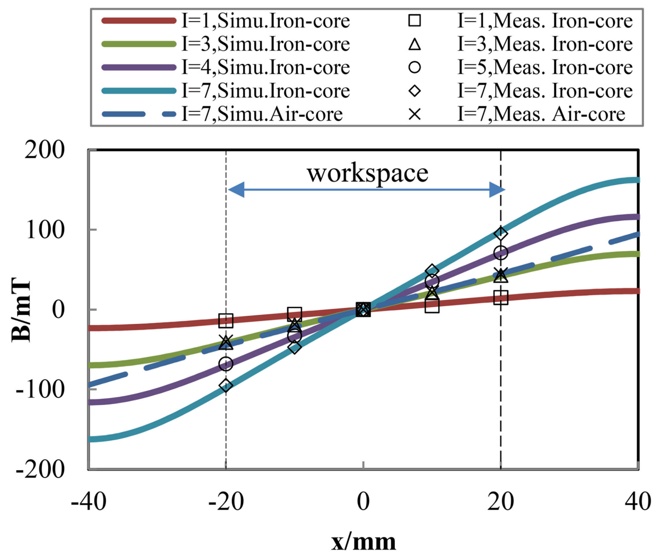

Fig. 9. Selection field generated by two DCCs with its axial axis located along the *x*-axis. Both sides of the coil load an equal and opposite current. Simulation results and measurements are marked by solid lines and scattered points, respectively. The field is highly linear in the workspace for iron-core and air-core coils. The slope of the curve indicates the gradient. The field gradients of the iron-core coils are much greater than those of the air-core coils. When a 3 A current is loaded onto the iron-core coils, the field gradient is comparable to that of the air-core coils with a 7 A current.

implemented the simulations with COMSOL Multiphysics software. The cores are located inside the inner coils of the DCCs. We devised an experiment to verify the suitability of the coil-core topology design for hybrid electromagnetic MNP actuation and imaging, as shown in Fig. 8. The two actuation coils with iron cores were powered by two dc power supplies (AMETEK SGA 600/17, 10 kW). A sinusoidal signal with a high frequency generated by a function generator (KEYSIGHT 33500B Series) was amplified by a power amplifier (AE TECHRON 7224), with the resultant current being fed to the excitation coil.

B. Effect of the Selection Field on the Coil-Core Structure

The magnetic field gradients in the air-core system and the iron-core system are compared in Fig. 9. The magnitude of the magnetic field gradient in the iron-core system at 3 A was almost equal to the magnitude of the magnetic field gradient in

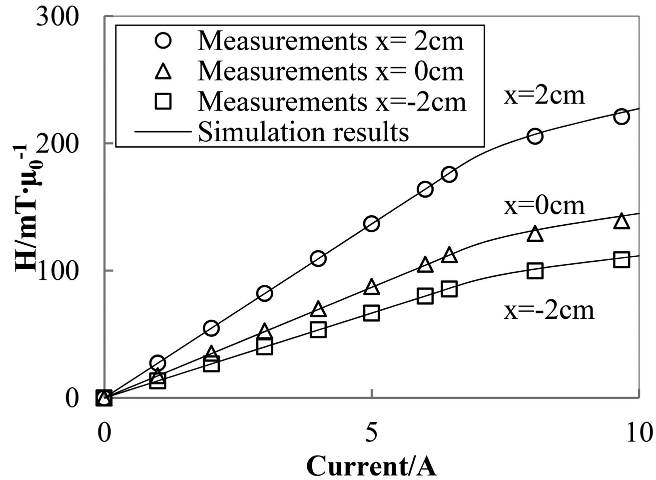

Fig. 10. Relationship between the magnetic field strength and the current in the iron-core system; the measurements were taken at the center of the workspace and at the two edges. The magnetic field strength is proportional to the input current.

the air-core system at 7 A. If the iron-core system was loaded at 7 A, the magnitude of the magnetic field gradient was almost 2.3 times that of the air-core system. One hypothesis is that the selection field G_x is linearly related to the workspace and constant in (3). Due to the linearity of the selection field within the workspace, we also regard G_x as a constant when using soft magnetic components in the proposed MPI system.

C. Effect of the Drive Field on the Coil-Core Structure

The sinusoidal currents loaded in the air-core coils can generate orthogonal sinusoidal fields for the FFP to scan a sinusoidal curve or a Lissajous trajectory depending on the linearity of the relationship between the current input and the field induction of the air-core coil. However, for the iron-core coil, the input current and field output will exhibit a complex relationship due to the nonlinear magnetization process of the core. Simulations and experiments were carried out to investigate this nonlinear relationship, and the results of the magnetic field of the iron-core coil with respect to the current are shown in Fig. 10.

The curve for the 7 A current contains an inflection point. The current and the magnetic field of the iron-core coil exhibited a linear relationship for currents smaller than 7 A, while the input and output showed a nonlinear relationship for currents larger than 7 A. This phenomenon is due to the nonuniform magnetization of the core. For currents lower than the inflection current, the whole core will maintain an unsaturation condition. However, part of the core will be saturated for currents higher than the inflection current, and reflect the nonlinearity of the outer field. Therefore, it is recommended that the linear condition of the iron-core coil, for currents lower than 7 A, be utilized in the current system. The hypothesis of (19) is that the magnetic field amplitude A_D and the input current amplitude I_{AC} have a linear relationship

$$A_D = p_D I_{\mathrm{AC}} \tag{19}$$

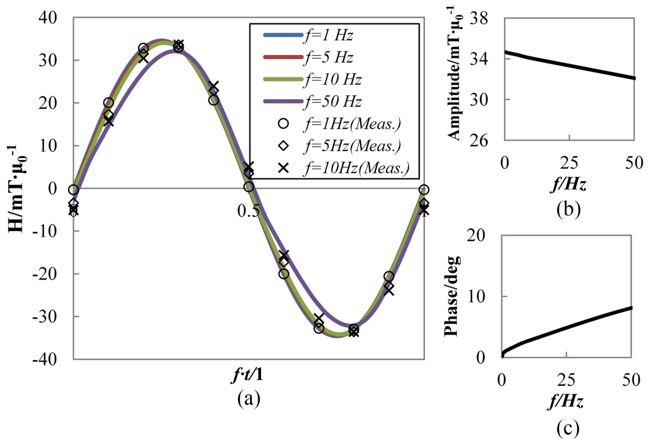

Fig. 11. Simulation and experimental results of magnetic field strength versus frequency. The sinusoidal currents are loaded onto the iron-core coils. They have the same amplitude but different frequency. (a) Magnetic field strength in different phases. (b) Amplitude decreases with respect to frequency. (c) Phase delay increases with respect to frequency.

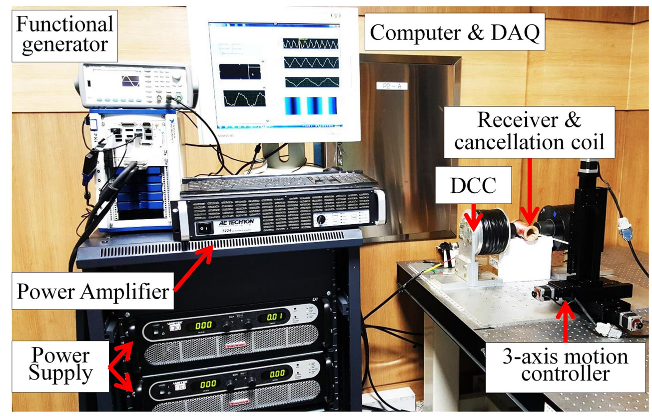

Fig. 12. Hardware connections for the proposed navigation system. Two power supplies, which are controlled separately by PC LabVIEW controller, supply currents to DCCs for generating FFP, moving FFP, and generating a magnetic gradient field to steer MNPs. A current generated by a function generator and amplified by a power amplifier is supplied to an excitation coil with low amplitude and high frequency. DAQ system is used to collect signals from a receiver coil and a cancellation coil.

where p_D is the sensitivity of the DCC and is independent of input current. If the current is lower than 7 A, the received signal in (14) can be directly applied in MPI with iron cores.

The trajectory is also affected by the low-frequency eddy currents in the core, which are induced by the low-frequency drive field. While using currents with the same amplitude but different frequency to achieve FFP scanning, the effective field for steering the FFP is dependent on the frequency, as shown in Fig. 11. Fig. 11(a) shows the magnitudes of the field in the time domain with different frequencies, and Fig. 11(b) shows that the amplitude of the magnetic field strength decreases with respect to the frequency. The amplitude of the low-frequency drive field in the time domain affects only the size of the workspace. If a higher low-frequency drive field frequency is needed, the amplitude of the currents should be increased slightly to maintain the size of the workspace. Furthermore, phase delays under different frequencies are shown in Fig. 11(c). If the frequency is less than 10 Hz, the phase delay of the magnetic field caused by the iron cores is less than 0.05 rad (about 2%). Therefore, the effects of the phase delay and the amplitude of the low-frequency drive field are insignificant and can be neglected in practice when the current frequency for the low-frequency drive field is lower than 10 Hz in the iron-core coil system.

D. Effects of the Excitation Field on the Coil-Core Structure

In the MPI mode, if the iron cores are simultaneously exposed to a strong selection field and a sufficiently low-amplitude high-frequency excitation field, their response can be approximated as the sum of the sinusoidal magnetization and the static magnetization. Moreover, even though the high-frequency excitation field can generate eddy currents on the skin of the core, we can consider the noise induced by the iron cores to be part of the empty signal, which is removed by the cancellation coil.

VI. Results of 1-D Navigation of MNPs and 2D Imaging

A. Experimental Set-Up for Navigation

In this section, we aim to implement the navigation system for MNPs using the iron-core electromagnetic system and iron-core compatible MPI scheme. Fig. 12 shows the hardware connections for the proposed navigation system. The nanoparticles used to verify the 1-D and 2-D MPI systems were 45–65 nm in diameter with a core size of 5–6 nm (Resovist). The Fe content and the magnetic susceptibility of the undiluted sample were about 58.6 mg/mL and 0.035 erg·G·g^{-1}, respectively, and saturation magnetization values were 340 $\pm$ 10 kA/m [32]. The length of the sample tank was 20 mm, and it was filled with 50 μL of undiluted MNP suspension and 570 μL of oil. The MNP suspension is water-based and does not mix with the oil. Therefore, the MNPs in the oil formed spherical droplets under the magnetic field, as shown in Fig. 13. In a previous work [24], we conducted experiments in a heterogeneous environment to determine the concentration distribution. In this paper, we used an oil environment because droplets in oil have an obvious bound surface and a stable volume. This is more convenient for comparing the guidance times and MPI images. The navigation system can steer the droplet along the x-axis (sample tank) and monitor the MNPs' positions in the real-time MPI images. We verified the real-time monitoring and steering results by observing the positions of the droplets with an optical camera.

B. 1D Particle Navigation

The MNPs were placed along the FFP scanning trajectory so that their concentration distribution could be monitored using MPI. Simultaneously, EMA mode steered the MNPs in the same direction inside the tube. We estimated the MNP concentration from the amplitude of the received signal. When a magnetic field was applied, the MNPs were aggregated into small droplets. In

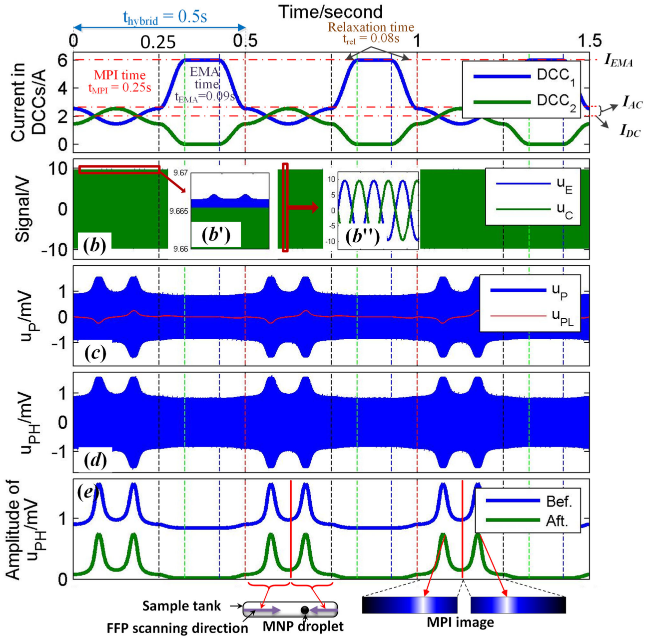

Fig. 13. 1D navigation results for MNPs with the following parameters: $t_{\text{hybrid}} = 0.5$ s; for the MPI period: $t_{\text{MPI}} = 0.25$ s, $I_{\text{DC}} = 2$ A, $I_{\text{AC}} = 0.88$ A; for the relaxation period: $t_{\text{rel}} = 0.08$ s; for the EMA period: $t_{\text{EMA}} = 0.09$ s, $I_{\text{EMA}} = 6$ A. (a) Waveforms of the currents in the DCCs. The relaxation times are also included to prevent voltage surges. (b) Comparison between u_E and u_C. At the full scale, there is an undetectable difference between u_E and u_C. (b') MNPs cause slight differences between the amplitudes of u_E and u_C. (b") Frequencies of u_E and u_C are the same, but their phases differ by 180°. (c) Low-frequency component $u_{PL}(t)$ and the total voltage $u_p(t)$ induced by the particles. As the excitation field and the low-frequecy drive field are perpendicular to each other, $u_p(t)$ has little effect on $u_{PL}(t)$. (d) High-frequency component $u_{PH}(t)$, whose amplitude is shown in (e). (e) The cancellation coil does not reduce the empty signal to exactly 0 V due to manufacturing errors. As the amplitude of the empty signal is consistent, we can subtract the amplitude of the empty signal from the amplitude of the main signal. The blue and green lines show the amplitude before and after the correction, respectively. The useful signal segments are those formed during the MPI mode. The MPI time includes two full MPI scanning periods in different directions. We can derive the full MNP distribution from each scan.

this experiment, the initial position of the droplet is on the left end of the tank, and a constant current was applied to the right coil to guide the droplet to the right using EMA mode. The droplet was monitored simultaneously using MPI mode. Guidance was terminated when the MNP droplet reached the right side of the tank. The resultant signals are shown in Fig. 13, and snapshots showing the locations of the MNPs during the MPI experiments are shown in Fig. 14. The positions of the droplets measured during the real-time MPI monitoring experiments are shown in Fig. 15.

The maximum values in the MPI image are thought to indicate the center of the MNP droplets. The grayscale images are reconstructed from the MPI images. These illustrate the concentrations of the MNPs, with black indicating an MNP concentration of zero.

The white regions in Fig. 14 indicate the highest MNP concentrations along the sample tank. The experimental results (see Fig. 14) verified that the navigation system can monitor the

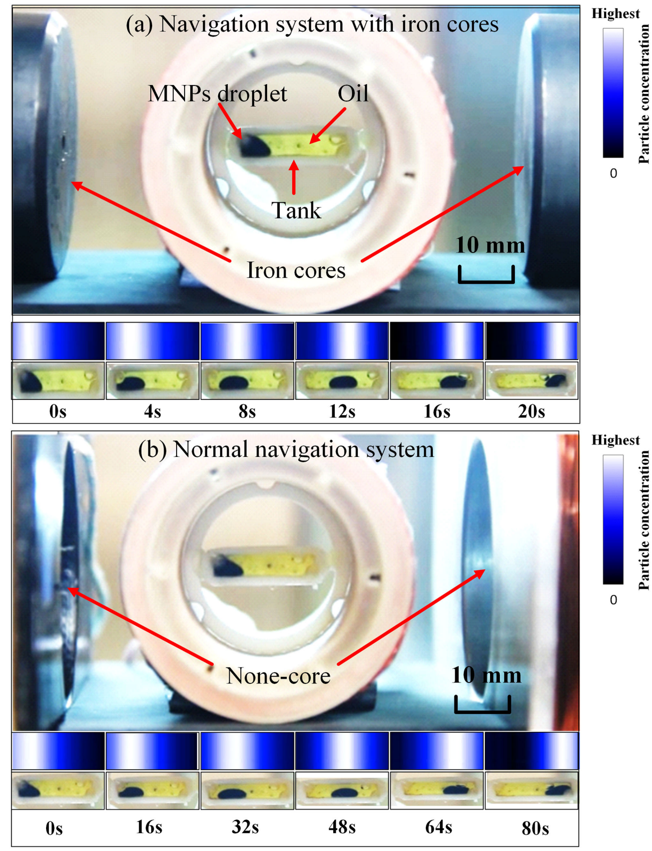

Fig. 14. Results of experiments using Resovist MNPs manipulated by the navigation system. During the EMA periods, the force was toward the right side of the sample tank [$I_{\text{EMA}} = 6$ A (3.12 T/m)] . The camera images and the MPI images (above the camera images) show the position of the particle droplet. The white regions indicate a higher MNP concentration. A magnetic field gradient of 1.04 T/m, induced by $I_{\text{DC}} = 2$A, was used in MPI mode. I_{AC} was set to 0.88 A to incorporate a workspace of 4 cm. The excitation field was 200 μT and 40 kHz. (a) Guidance by a navigation system with iron cores. (b) Guidance by a normal navigation system.

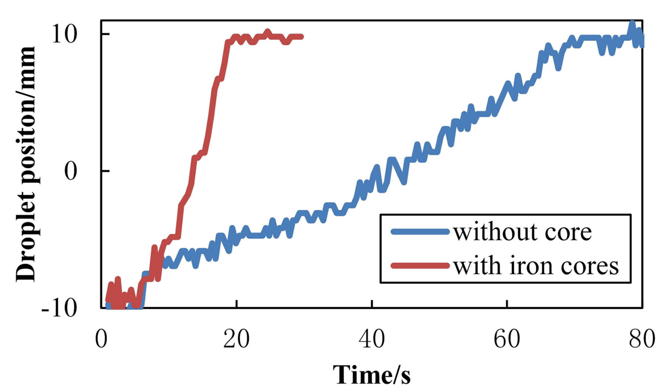

Fig. 15. Positions of the MNP droplets during navigation with and without cores.

positions of MNPs and feed particle concentration information back to the EMA mode, which then guides MNPs to the expected locations. Our 1-D MNP navigation system had a 2-Hz system refresh frequency (repetition frequency), and the MPI image frame and control field were updated every 0.5 s, which

TABLE II
GUIDANCE TIMES OF MNPS WITH AND WITHOUT CORES INSIDE A SAMPLE TANK

I_{AC}	I_{DC}	I_{EMA}	*With cores*	*Without cores*
0.88A	2A	6A	20 sec	80 sec
		5A	34 sec	105 sec
		4A	48 sec	140 sec
		3A	82 sec	190 sec
1.76A	4A	6A	16 sec	66 sec
		5A	33 sec	81 sec
		4A	40 sec	100 sec
		3A	68 sec	150 sec

is an appropriate bandwidth for navigating capillaries in the brain where the velocity of blood is approximately 1 mm/s [33]. The same current conditions were applied in the navigation systems with and without iron cores to observe the steering force effects of the iron core for the conditions shown in Fig. 2. The durations for guiding the MNP droplets from the left to the right of the tank are given in Table II. I_{EMA} was increased to speed up the MNPs during EMA modes, while I_{AC} was adjusted to maintain the size of workspace at 4 cm. The results show that by installing the soft magnetic cores, guidance time can be significantly reduced and real-time MPI imaging is still available by utilizing the proposed AM MPI scheme with higher imaging resolution.

To extend the 1-D navigation system to a 3-D system, two sets of iron-core coils, which can induce fields orthogonal to each other, should be included in the proposed system. These coils can act as the actuation coils in the EMA to steer MNPs in a 3-D target region and the drive coils in the MPI mode to monitor MNP distribution. By choosing currents of appropriate frequency in these two sets of coils, a 3-D Lissajous trajectory can be achieved to cover a 3-D workspace, and the received signal can then be reconstructed to form 3-D MPI images. We estimated that if we utilized 24- and 20-Hz sinusoidal currents in these two sets of coils during the MPI periods, the navigation system would retain a 2-Hz system refresh frequency. When the frequency of the drive field is higher than 10 Hz, phase delays can affect the receiver signal. To remove these phase delay effects, the measured signal can be deconvolved with the estimated time constant, which reveals the underlying mirror symmetry [34]. Through this compensation, an exact image of MNPs in the 3-D system can be obtained. All of these conditions are possible with our current power supply with a current slew rate of 153 A/s.

C. 2D Imaging

Fig. 16 shows 2-D images with different gradients. For this experiment, EMA mode was deactivated and the navigation system had a 1-D MPI functionality: Only MNPs along the DCC (x) axis can be scanned (see Fig. 2). The MPI scanning frequency in our system was 10 Hz, and a three-axis motion controller (st1, Korea) was used to move a 2-D sample (see Fig. 16) at a constant velocity through the DCC axis. The movement

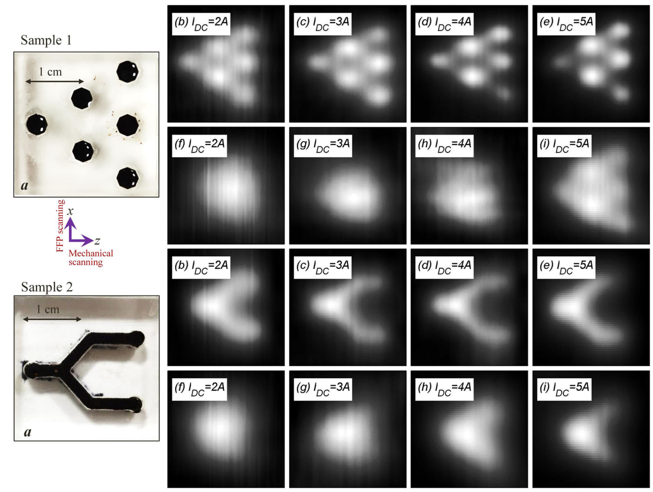

Fig. 16. Reconstructed images of the objects for two samples. Sample 1: MPI images of six Resovist MNPs droplets, each droplet contains 10 μL of Resovist MNPs. Sample 2: Images of a Y-shaped channel with a diameter of 1 mm. (a) Sample. (b)–(e) Results generated from the iron-core MPI system. (f)–(i) Results created from the MPI system without a core. The results under the same current conditions in two systems are compared. For the system without a core, when the current was too low, the gradient was not sufficient to generate clear images (f)–(h). For different I_{DC}, the excitation fields for different scans were maintained at 200 μT and 40 kHz. For $I_{\text{DC}} = 5$ A, the resultant gradient field G_x was 2.6 T/m. The sampling times were 15 s.

direction was along the z-axis of the receiver coil, as shown in Fig. 2. In the experiments, the velocity was set to 2 mm/s, and the sampling time for each image was 15 s. While maintaining the excitation fields for different scans at 200 μT and 40 kHz, the images became clear when I_{DC} was increased.

The 2-D MPI images created from two samples are shown in Fig. 16. In each figure, (a) shows the samples, (b)–(e) show the images from iron-core MPI, and (f)–(i) show the images from MPI without cores. Sample (1) shows MPI images of six Resovist MNP droplets, with each droplet containing 10 μL of Resovist MNPs. The gradient field had a positive effect on MPI image resolution, as the gradient increased, each droplet became clearer. Sample (2) in Fig. 16 shows images of a Y-shaped channel, which simulates bifurcation of a small blood vessel. To steer the MNPs, we can combine this MPI image with EMA periods. The MPI images generated by MPI systems with cores are exceptionally clearer than the MPI images generated by MPI systems without cores. When using the same MNPs, the FWHM resolution, which is the intrinsic resolution estimated from the gradient of the selection field, is inversely proportional to the gradient. When the cores were used, the imaging resolution improved by a factor of 0.43. Based on [17], the MPI resolution can reach 1 mm when the effective aggregation diameter is 24 nm [27]. We can also improve the resolution further by using bigger MNPs, or increasing the magnetic gradient field [17].

These results show that there are three major benefits to the proposed MPI method: improved resolution without increasing the amplitude of the high-frequency magnetic field, retaining the ability to conduct MPI when using iron cores, and generating the same gradient using less electrical energy than an air-core coil system. These features are all beneficial for extending the applicability of MPI using a low-cost method.

VII. Conclusion

A navigation system with iron cores is proposed, which is cost-efficient, compact, and optimized for precise targeting of MNPs by implementing real-time actuation and monitoring. The design is suitable for a low-blood-speed application. These novel techniques can be adapted for a variety of applications, particularly direct delivery of nanomedicines. The proposed system can allow a user to manipulate MNPs in response to real-time MPI images. By mixing two frequency fields, the proposed AM MPI scheme makes soft magnetic components accessible to an MPI system. Soft magnetic components can enhance the magnetic field gradient and strength, and provide a higher steering force for MNPs and enhanced MPI resolution. The electromagnetic system with iron-cores can save up to 67% of the required current as compared to a system without cores. Thus, the quantity of heat generated is only one-ninth of that of the noncore system. In addition to the higher gradient field due to the iron cores, the narrow-band receiver coil, the low-amplitude excitation field, the low-frequency drive field, and the current savings make the proposed MPI highly scalable. For *in vivo* imaging at the human scale, several design improvements and innovations must be introduced to the present system. Real-time implementation of a mouse-sized system and experiments in a vascular network with many bifurcations using an intuitive tele-manipulation scheme will be studied in future works.

References

[1] S. C. McBain, H. H. Yiu, and J. Dobson, "Magnetic nanoparticles for gene and drug delivery," *Int. J. Nanomedicine*, vol. 3, no. 2, pp. 169–180, 2008.

[2] B. Gleich and J. Weizenecker, "Tomographic imaging using the nonlinear response of magnetic particles," *Nature*, vol. 435, no. 7046, pp. 1214–1217, 2005.

[3] F. Dilnawaz and S. K. Sahoo, "Therapeutic approaches of magnetic nanoparticles for the central nervous system," *Drug Discovery Today*, vol. 20, no. 10, pp. 1256–1264, 2015.

[4] J. Bar, R. S. Herbst, and A. Onn, "Targeted drug delivery strategies to treat lung metastasis," *Expert Opinion Drug Del.*, vol. 6, no. 10, pp. 1003–1016, 2009.

[5] V. P. Torchilin, "Passive and active drug targeting: Drug delivery to tumors as an example," *Drug Delivery*. New York, NY, USA: Springer-Verlag, 2010, pp. 3–53.

[6] F. U. Amin *et al.*, "Osmotin-loaded magnetic nanoparticles with electromagnetic guidance for the treatment of Alzheimer's disease," *Nanoscale*, vol. 9, no. 30, pp. 10619–10632, 2017.

[7] I. S. Khalil, P. Ferreira, R. Eleutério, C. L. de Korte, and S. Misra, "Magnetic-Based closed-loop control of paramagnetic microparticles using ultrasound feedback," in *Proc. IEEE Int. Conf. Robot. Autom.*, 2014, pp. 3807–3812.

[8] I. S. Khalil, J. D. Keuning, L. Abelmann, and S. Misra, "Wireless magnetic-based control of paramagnetic microparticles," in *Proc. 4th IEEE RAS EMBS Int. Conf. Biomed. Robot. Biomechatronics*, 2012, pp. 460–466.

[9] J. Yu, T. Xu, Z. Lu, C. I. Vong, and L. Zhang, "On-demand disassembly of paramagnetic nanoparticle chains for microrobotic cargo delivery," *IEEE Trans. Robotics*, vol. 33, no. 5, pp. 1213–1225, Oct. 2017.

[10] J. B. Mathieu and S. Martel, "Steering of aggregating magnetic microparticles using propulsion gradients coils in an MRI scanner," *Magnetic Resonance Med.*, vol. 63, no. 5, pp. 1336–1345, 2010.

[11] S. Martel, "Combining pulsed and DC gradients in a clinical MRI-based microrobotic platform to guide therapeutic magnetic agents in the vascular network," *Int. J. Adv. Robot. Syst.*, vol. 10, no. 1, pp. 30–37, 2013.

[12] X. Yan *et al.*, "Multifunctional biohybrid magnetite microrobots for imaging-guided therapy," *Sci. Robot.*, vol. 2, no. 12, pp. 1–14, 2017.

[13] L. Arcese, M. Fruchard, and A. Ferreira, "Endovascular magnetically guided robots: Navigation modeling and optimization," *IEEE Trans. Biomed. Eng.*, vol. 59, no. 4, pp. 977–987, Apr. 2012.

[14] K. B. Yesin, K. Vollmers, and B. J. Nelson, "Modeling and control of untethered biomicrorobots in a fluidic environment using electromagnetic fields," *The Int. J. Robot. Res.*, vol. 25, no. 5–6, pp. 527–536, 2006.

[15] J. Borgert *et al.*, "Fundamentals and applications of magnetic particle imaging," *J. Cardiovascular Comput. Tomography*, vol. 6, no. 3, pp. 149–153, 2012.

[16] J. Haegele *et al.*, "Magnetic particle imaging: visualization of instruments for cardiovascular intervention," *Radiology*, vol. 265, no. 3, pp. 933–938, 2012.

[17] P. W. Goodwill and S. M. Conolly, "The X-space formulation of the magnetic particle imaging process: 1-D signal, resolution, bandwidth, SNR, SAR, and magnetostimulation," *IEEE Trans. Med. Imaging*, vol. 29, no. 11, pp. 1851–1859, Nov. 2010.

[18] E. M. Cherry, P. G. Maxim, and J. K. Eaton, "Particle size, magnetic field, and blood velocity effects on particle retention in magnetic drug targeting," *Med. Phys.*, vol. 37, no. 1, pp. 175–182, 2010.

[19] M. D. Tehrani, M. O. Kim, and J. Yoon, "A novel electromagnetic actuation system for magnetic nanoparticle guidance in blood vessels," *IEEE Trans. Magnetics*, vol. 50, no. 7, pp. 1–12, Jul. 2014.

[20] M. Latulippe and S. Martel, "Dipole field navigation: Theory and proof of concept," *IEEE Trans. Robot.*, vol. 31, no. 6, pp. 1353–1363, Dec. 2015.

[21] B. Shapiro, S. Kulkarni, A. Nacev, S. Muro, P. Y. Stepanov, and I. N. Weinberg, "Open challenges in magnetic drug targeting," *Wiley Interdisciplinary Reviews: Nanomedicine Nanobiotechnology*, vol. 7, no. 3, pp. 446–457, 2015.

[22] I. N. Weinberg *et al.*, "Increasing the oscillation frequency of strong magnetic fields above 101 kHz significantly raises peripheral nerve excitation thresholds," *Med. Phys.*, vol. 39, no. 5, pp. 2578–2583, 2012.

[23] P. W. Goodwill, G. C. Scott, P. P. Stang, and S. M. Conolly, "Narrowband magnetic particle imaging," *IEEE Trans. Med. Imaging*, vol. 28, no. 8, pp. 1231–1237, Aug. 2009.

[24] X. Zhang, T.-A. Le, and J. Yoon, "Development of a real time imaging-based guidance system of magnetic nanoparticles for targeted drug delivery," *J. Magnetism Magnetic Mater.*, vol. 427, pp. 345–351, 2017.

[25] A. Mahmood, M. Dadkhah, M. O. Kim, and J. Yoon, "A novel design of an MPI-based guidance system for simultaneous actuation and monitoring of magnetic nanoparticles," *IEEE Trans. Magnetics*, vol. 51, no. 2, pp. 1–5, Feb. 2015.

[26] D. Thapa, V. Palkar, M. Kurup, and S. Malik, "Properties of magnetite nanoparticles synthesized through a novel chemical route," *Mater. Lett.*, vol. 58, no. 21, pp. 2692–2694, 2004.

[27] N. Panagiotopoulos *et al.*, "Magnetic particle imaging: Current developments and future directions," *Int. J. Nanomedicine*, vol. 10, pp. 3097–3114, 2015.

[28] T. Knopp and T. M. Buzug, *Magnetic particle imaging: An introduction to imaging principles and scanner instrumentation*. Heidelberg, Germany: Springer, 2012.

[29] V. Schulz, M. Straub, M. Mahlke, S. Hubertus, T. Lammers, and F. Kiessling, "A field cancellation signal extraction method for magnetic particle imaging," *IEEE Trans. Magnetics*, vol. 51, no. 2, pp. 1–4, Feb. 2015.

[30] J. Weizenecker, J. Borgert, and B. Gleich, "A simulation study on the resolution and sensitivity of magnetic particle imaging," *Phys. Med. Biology*, vol. 52, no. 21, pp. 6363–6374, 2007.

[31] VACUUM-SCHMELZE GmbH & Co, "Soft magnetic cobalt-iron-alloys," KG, Hanau, Germany, 2001. [Online]. Available: https://www.vacuumschmelze.com/fileadmin/Medienbiliothek_2010/Downloads/HT/PHT_004_CoFe.pdf. [Accessed: Jun. 12, 2018].

[32] D. Eberbeck, F. Wiekhorst, S. Wagner, and L. Trahms, "How the size distribution of magnetic nanoparticles determines their magnetic particle imaging performance," *Appl. Phys. Lett.*, vol. 98, no. 18, 2011, Art. no. 182502.

[33] K. Ivanov, M. Kalinina, and Y. I. Levkovich, "Blood flow velocity in capillaries of brain and muscles and its physiological significance," *Microvascular Res.*, vol. 22, no. 2, pp. 143–155, 1981.

[34] M. Utkur, Y. Muslu, and E. U. Saritas, "Relaxation-based viscosity mapping for magnetic particle imaging," *Phys. Med. Biology*, vol. 62, no. 9, pp. 3422–3439, 2017.

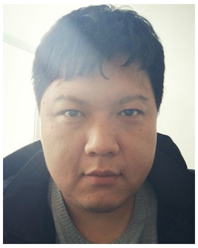

Xingming Zhang received the Ph.D. degree in marine engineering from Dalian Maritime University, Dalian, China, in 2014.

He was a Senior Researcher with Gyeongsang National University, Jinju, South Korea. He is currently a Lecturer with the Harbin Institute of Technology, Weihai, PRC. His current research interests include the magnetic particle imaging (MPI), MPI-based nano-robot control, and microparticle sensor.

Tuan-Anh Le received the M.Sc. degree in electrical engineering from the Hanoi University of Science and Technology, Hanoi, Viet Nam, in 2013. In 2018, he joined the School of Integrated Technology, Gwangju Institute of Science and Technology, Gwangju, Korea, where he is currently working toward the Ph.D. degree. From 2014 to 2017, he was a Researcher and Ph.D. candidate in Gyeongsang National University, Jinju, South Korea. His current research interests include electromagnetics, actuators, magnetic particle imaging, and bio-nano robot control.

Ali Kafash Hoshiar received the Ph.D. degree in mechanical engineering from the Islamic Azad University of Science and Research Branch, Tehran, in 2014.

Since 2009, he has been a Faculty Member with Islamic Azad University of Qazvin. From 2015 to 2017, he was a Senior Researcher with Gyeongsang National University. His research interests focused on Micro robotics /Nanorobotics for biomedical applications.

Jungwon Yoon (M'05) received the Ph.D. degree in mechatronics from the Gwangju Institute of Science and Technology, Gwangju, South Korea, in 2005.

From 2005 to 2017, he was a Professor with the School of Mechanical and Aerospace Engineering, Gyeongsang National University, Jinju, South Korea. In 2017, he joined the School of Integrated Technology, Gwangju Institute of Science and Technology, Gwangju, Korea, where he is currently an Associate Professor. His current research interests include bionanorobot control, virtual reality haptic devices, and rehabilitation robots. He has authored or coauthored more than 85 peer-reviewed journal articles and patents.

Dr. Yoon is a Technical Editor for the IEEE/ASME TRANSACTIONS ON MECHATRONICS and an Associate Editor for *Frontiers in Robotics and AI*.